Journal of the Meteorological Society of Japan

EARLY ONLINE RELEASE

The DOI for this manuscript is

DOI:10.2151/jmsj.2023-021

J-STAGE Advance published date: May 16th, 2023

The Application of FY-3D/E Meteorological Satellite Products in South China Sea Summer Monsoon Monitoring

Suling REN

National Satellite Meteorological Center / National Center for Space Weather, China Meteorological Administration, Beijing, China
Innovation Center for FengYun Meteorological Satellite(FYSIC), Beijing, China
Key Laboratory of Radiometric Calibration and Validation for Environmental Satellites, China Meteorological Administration, Beijing, China

Xiang FANG[1]

National Meteorological Center, China Meteorological Administration, Beijing, China

Ning NIU

China Meteorological Administration Training Center, Beijing, China

and

Wanjiao SONG

National Satellite Meteorological Center / National Center for Space Weather, China Meteorological Administration, Beijing, China
Innovation Center for FengYun Meteorological Satellite(FYSIC), Beijing, China
Key Laboratory of Radiometric Calibration and Validation for Environmental Satellites, China Meteorological Administration, Beijing, China

December 12, 2022

----

1) Corresponding author: Xiang Fang, National Meteorological Center, China Meteorological Administration, Zhongguancun Nandajie 46, Haidian District, Beijing 100081, China
Email: fangx@cma.gov.cn
Tel: +86-13011035305

Abstract

Based on the vertical atmospheric sounding system carried by the FY-3D meteorological satellite (FY-3D/VASS) and the new wind radar instrument carried by the FY-3E meteorological satellite (FY-3E/WindRAD), a study of the potential application of research on the changes of temperature, humidity, and ocean wind vector (OWV) during the onset of the South China Sea summer monsoon (SCSSM) was carried out. The applications of these satellite datasets in SCSSM monitoring was evaluated, and the SCSSM onset process in 2022 was analyzed. The results showed that the mean bias of the FY-3D/VASS temperature and specific humidity at 850hPa, compared with that of the fifth-generation ECMWF reanalysis, were -0.6 K and -0.53 g kg^{-1}, respectively, and the pseudo-equivalent potential temperature (θ_{se}) was slightly lower, by 1-2 K; the distribution of θ_{se} was consistent with the seasonal advancement of the SCSSM. Compared with Metop-C/ASCAT, the mean bias of FY-3E/WindRAD zonal wind was positive and that of meridional wind was negative. The correlation coefficient, mean bias, mean absolute error, and root-mean-square error of the wind speed were 0.79, -0.45 m s^{-1}, 1.56 m s^{-1}, and 2.03 m s^{-1}, respectively. The distributions of OWV were consistent, and the region and intensity of strong wind speed were close to each other. The temperature, humidity, and wind reversal during the onset of the SCSSM in 2022 were well-monitored by the FY-3D/E-derived θ_{se} and OWV dual indices, which are consistent with the SCSSM onset date, the third pentad in May, issued officially by the National Climate Center, China Meteorological Administration. Before the SCSSM onset in 2022, the tropical storms' pumping effect in early May increased the

westerly wind over the tropical ocean north of the equator. After the storm weakened, the southwesterly wind passed across the Indochina Peninsula and reached South China Sea, causing the SCSSM onset.

Keywords FY-3D/VASS temperature and humidity; FY-3E/WindRAD ocean wind vector; South China Sea summer monsoon; pseudo-equivalent potential temperature

1. Introduction

Asia and Australia are typical monsoon regions, forming the Asian–Australian monsoon system. The onset of the summer monsoon indicates that the atmospheric circulation changes from winter to summer. The Asian summer monsoon includes the tropical summer monsoon and subtropical summer monsoon (Wu and Zhang 1998; Wu et al. 2013a; Wu et al. 2013b). The onset of the Asian tropical summer monsoon generally passes through three stages. First, the Asian summer monsoon is established over the south of the Bay of Bengal. Then, in mid-May, it extends eastward through the Indochina Peninsula to the South China Sea summer monsoon (SCSSM) region. Finally, the onset of the South Asian summer monsoon arrives in June. The onset of the SCSSM indicates that the East Asian subtropical summer monsoon has begun to establish itself, and the primary rainy season begins (Chen et al. 2022). In addition, this marks a major transition in the seasonal change of climate in Asia, and can affect the weather and climate in other regions of the world through atmospheric teleconnection (Xu et al. 2019). Therefore, the South China Sea Monsoon Experiment (SCSMEX) was carried out more than 20 years ago to conduct in-depth research on the onset and evolution of the SCSSM (Lau et al. 1998; Chan et al. 2002; Wang 2008).

The studies on the SCSSM mainly investigated the dynamics and triggering mechanism of its onset, the characteristics and mechanisms of the multiple time-scale changes of the onset of the summer monsoon, and the monitoring indices. These studies demonstrated that during the onset of the SCSSM, the large-scale atmospheric circulation in Asia changes suddenly; the South Asia High jumps rapidly to the north, the tropospheric atmosphere in the southeast of the Tibet Plateau and the eastern parts of China warms rapidly, and the atmospheric heating source and water vapor sink increase significantly (Jiang and Luo 1995; Wang et al. 2018). An explosive vortex or cyclone storm in the Bay of Bengal or a tropical cyclone in the northwest Pacific are important trigger factors for the onset of the SCSSM (Wu et al. 2011, 2012, 2013a, and 2013b; Ren et al. 2016). In addition, the southward motion of a middle- and high-latitude cold front can also trigger the onset of the SCSSM (Ding and Liu 2001).

To study the characteristics of the onset of the SCSSM, it is necessary to define the monitoring indices. Most indices are established with single or multiple parameters of wind, temperature, precipitation, convection, and their derived parameters, forming a single or comprehensive index (Li and Zhang 1999). While the average onset dates produced by different indices are fairly consistent, due to the complexity of the onset process of the summer monsoon, they often produce different dates in a particular year. Zhang et al. (2003) defined the East Asian summer monsoon index by using zonal wind at 850 hPa, and Webster and Yang (1992) studied the Asian summer monsoon index by using the vertical zonal wind shear between high and low troposphere. The satellite data regarding outgoing longwave radiation (OLR) or blackbody brightness temperature (TBB), combined with the meteorological reanalysis data, are usually used to define the SCSSM indices and, generally, two indices are used to determine summer monsoon activity (Ding and Li 1999; He et al. 1996; Liang et al. 1999; Guo et al. 1999; Liu et al. 1998; Jiang et al. 2006). In addition, Qian and Zhu (2001) and Zhu et al. (2001) studied the characteristics of deep convection, before and after the onset of the Asian summer monsoon, using the brightness temperature of the satellite water vapor channel in the upper troposphere, and demonstrated that the critical value of deep convection is 244 K, indicating that meteorological satellite data can be used to monitor the characteristics of significant changes in atmospheric temperature and humidity during the onset of the SCSSM. Ren and Fang (2013) and Ren et al. (2018) studied the application of meteorological satellite-derived atmospheric motion vector (AMV) and TBB in summer monsoon monitoring, indicating that satellite AMV and TBB double indices can better describe the characteristics of the onset of the SCSSM than a single convective index. In addition, the operational monitoring indices and determination methods for real-time monitoring of the SCSSM, based on AMV and TBB and carried out in real time, have been implemented as a component of operational climate services at the National Satellite Meteorological Center (NSMC), Chinese Meteorological Administration (CMA) (Ren et al. 2017). In the National Climate Center (NCC), CMA, zonal wind, and pseudo-equivalent potential temperature (θ_{se}) at 850hPa from the numerical prediction model, or reanalysis data, are used to calculate the SCSSM indices and the SCSSM intensity classification and carry out the prediction, monitoring, and impact assessment of the SCSSM (Shao et al. 2021).

The onset process of the Asian tropical summer monsoon occurs over the ocean with few conventional meteorological observations. The vertical atmospheric sounding system—including three instruments: the MicroWave Humidity Sounder (MWHS), MicroWave Temperature Sounder (MWTS), and Hyperspectral InfraRed Atmospheric Sounder (HIRAS)—carried by the FY-3D polar-orbiting meteorological satellites (FY-3D/VASS) can effectively observe the three-dimensional temperature and humidity of the atmosphere under all weather conditions (Gu et al. 2010; Guo et al. 2014; Zhang et al. 2021; Xian et al. 2021), and has played an important role in the monitoring of extreme weather events (Zhuang 2022; Ren et al. 2022). The application of this observation data in the monitoring of the SCSSM has great potential. The wind radar carried by the FY-3E meteorological satellite launched in 2021 can observe the global ocean surface wind field (FY-3E/WindRAD) (Zhang et al. 2022). Previous analysis has shown that, compared with the wind at 850 hPa, the surface wind can better describe the characteristics of the Asian monsoon (Wu et al. 2013b). Therefore, this paper will also evaluate the potential application of the FY-3E/WindRAD ocean surface wind in SCSSM monitoring.

This paper will focus on the evaluation of the applications of the FY orbiting meteorological satellite's retrieval of temperature, humidity, and ocean surface wind data in SCSSM monitoring. First, the performance of satellite data was evaluated during the key period of the onset of the summer monsoon in the SCSSM region, and summer monsoon indices retrieved by the satellites were compared to the operational indices of the NCC, CMA. Then, the SCSSM onset process in 2022 was studied using FY-3D/VASS and FY-3E/WindRAD data.

2. Data and Method

2.1 FY-3D/VASS temperature and humidity

The FY-3D meteorological satellite was launched on 15 November 2017 (Gu et al. 2010; Guo et al. 2014; Zhang et al. 2021; Xian et al. 2021). In this paper, the temperature and humidity data retrieved by the FY-3D/VASS were used. In total, there are 3 vertical atmospheric sounding instruments, including 4-channel MWHS, 5-channel MWTS, and 1370-channel HIRAS. A package has been developed to retrieve the atmospheric temperature and humidity profile, in both clear and cloudy atmospheres, from the VASS measurements. The algorithm that retrieves these parameters contains four steps: 1) cloud and precipitation detection, 2) bias adjustment for VASS measurements, 3) regression retrieval processes, and 4) a nonlinear iterative physical retrieval. The VASS temperature and humidity data cover the entire world, with a maximum spatial resolution of 15 km. There are 43 pressure layers, from 1013.25 to 0.1 hPa. The pressure layer selected in this paper is near 850 hPa.

Because it is affected by hydrometeors, temperature and humidity estimation accuracy may be relatively low. The FY-3D/VASS temperature and humidity datasets provide a data quality flag (quality flag is 0 or 1; 0 is for good); the data with quality flag number 0 was chosen in this research.

2.2 FY-3E/WindRAD ocean wind vector

The FY-3E, the world's first early morning orbit meteorological satellite, was successfully launched in July 2021. The satellite is equipped with 11 remote sensing instruments, including 3 that are newly developed, 7 that have been upgraded, and 1 that is inherited (Zhuang 2022; Zhang et al. 2022). The FY-3E is capable of an active and passive combination of ocean surface wind detection capability, and has now added dual-frequency wind radar using C-band (5.3 GHz) and Ku-band (13.265 GHz), the first active remote sensing instrument loaded on the FY series meteorological satellite. This instrument can provide high-precision measurement of global ocean surface wind, including wind speed and wind direction. The ocean wind vector (OWV) from FY-3E/WindRAD has become a stable operational product since 1 March 2022.

The daily OWV selected in this paper is divided into ascending and descending orbit. The spatial resolution is 0.25° (latitude) × 0.25° (longitude), covering the global ocean surface. In this paper, the daily ascending and descending orbit data is processed into daily averages. The satellite observation time of the SCSSM region is about 1000 and 2200 UTC.

2.3 Metop/ASCAT ocean wind vector

The Advanced SCATterometer (ASCAT) is one of the instruments carried onboard the Meteorological Operational (Metop) polar satellites launched by the European Space Agency (ESA) and operated by the European Organisation for the Exploitation of Meteorological Satellites (EUMETSAT) (Verhoef et al. 2012; Verspeek et al. 2019). Metop-C was launched on 7 November 2018. Horizontal stress-equivalent wind vector was measured at 10 m height and included wind speed and wind direction. Wind speed was measured in m s^{-1}. The wind speed range was from 0-50 m s^{-1}, but the wind speeds exceeding 25 m s^{-1} are generally less reliable (OSI SAF/EARS Winds Team 2021). The accuracy should be better than 2 m s^{-1} in wind component standard deviation, with a bias of less than 0.5 m s^{-1} in wind speed. The spatial resolution was about 12.5 km, observed twice each day. In this paper, the data were processed into daily averages, with a spatial resolution of 0.25° (latitude) × 0.25° (longitude). The satellite observation time of the SCSSM region was about 0200 and 1400 UTC.

2.4 ERA5 reanalysis data

The temperature, humidity, and wind data used in this paper are from the European Centre for Medium-Range Weather Forecasts (ECMWF) reanalysis dataset (ERA5), which combines numerical model and global observation data, with a horizontal spatial resolution of 0.25º (longitude) × 0.25º (latitude) and a temporal resolution of 1h. The daily averages data are processed in this paper, and the pressure layer used in this paper is 850 hPa (Hersbach et al. 2020).

2.5 Calculation Method of SCSSM Index

This paper carries out evaluation of FY-3D/VASS and FY-3E/WindRAD applications in SCSSM monitoring based on the indices operated by the NCC, CMA, including regional average pseudo-equivalent potential temperature index and regional average zonal wind index (Shao et al. 2021). The pseudo-equivalent potential temperature was calculated using Equations (1)-(4) (Bolton 1980):

$$e = prs \times q / \left(0.62197 + q\right) \tag{1}$$

$$tlcl = 55.0 + 2840.0 / \left(3.5 \times \log T - \log e - 4.805\right) \tag{2}$$

$$\theta = T \times \left(1000 / prs\right)^{0.2854 \times (1.0 - 0.28 \times q)} \tag{3}$$

$$\theta_{se} = \theta \times e^{\left(\frac{3376}{tlcl} - 2.54\right) \times q \times (1.0 + 0.81 \times q)} \tag{4}$$

where θ_{se} is the pseudo-equivalent potential temperature , θ is the potential temperature , *prs* is equal to 850 hPa, *tlcl* is the lifting condensation level temperature, *e* is water vapor pressure, *T* is the temperature (unit: K), and *q* is the mixing ratio (unit: kg kg^{-1}).

The region of the SCSSM is (10 º N-20 º N; 110 º E-120 º E) and the pseudo-equivalent potential temperature index is its regional average at 850 hPa. The wind index is the zonal wind regional average at 850 hPa used by the NCC, CMA. In this study, the zonal components of OWV from FY-3E/WindRAD were used as a replacement of the zonal wind at 850 hPa in the SCSSM wind index.

2.6 Evaluation method

The mean bias (MB), mean absolute error (MAE), root-mean-square error (RMSE), and correlation coefficient (CC) were calculated from Equations (5)-(8):

$$MB = \frac{1}{n}\sum_{i=1}^{n}(Y_i - X_i) \quad (5)$$

$$MAE = \frac{1}{n}\sum_{i=1}^{n}|Y_i - X_i| \quad (6)$$

$$RMSE = \sqrt{\frac{1}{n}\sum_{i=1}^{n}(Y_i - X_i)^2} \quad (7)$$

$$CC = \sum_{i=1}^{n}[(Y_i - \overline{Y})(X_i - \overline{X})] / \sqrt{\sum_{i=1}^{n}(Y_i - \overline{Y})^2 \sum_{i=1}^{n}(X_i - \overline{X})^2} \quad (8)$$

where *Y* is the evaluated variable, *X* is the reference variable, *n* is the matching sample number, $\overline{Y}$ is the average value of *n* samples of the evaluated variable, and $\overline{X}$ is the average value of *n* samples of the reference variable.

3. Results

3.1 FY-3D/VASS temperature and humidity evaluation in SCSSM monitoring

In this paper, the evaluation of the FY-3D meteorological satellite data was carried out for the 850 hPa pseudo-equivalent potential temperature index of the SCSSM, including temperature, humidity, and the pseudo-equivalent potential temperature calculated by Equations (1)-(4).

The scatter density and evaluation indices of the temperature at 850hPa between FY-3D/VASS and ERA5 in the SCSSM region (10°N -20°N; 110°E -120°E) in April, May, and June 2022 show that the matching sample number is about 80000, and the maximum matching sample number is about 86000 in May (Fig. 1). The lowest MB and MAE measurements in the 3 months occurred in April: -0.39 K and 1.02 K, respectively. The maximum CC was 0.46, which was also in April (Fig. 1a). The average MB in May was -0.73 K, the MAE was 1.11 K, and the minimum RMSE was about 1.54 K (Fig. 1b). The minimum CC was 0.27 in June (Fig. 1c). On the whole, the scatter density distribution from April to June shows that the FY-3D/VASS temperature at 850 hPa was abnormally high or low for some points. In these 3 months, the average MB was -0.64 K, MAE was 1.09 K, and RMSE was 1.61 K (Fig. 1d).

The scatter density and evaluation indices of the specific humidity at 850hPa between FY-3D/VASS and ERA5 in the SCSSM region (10°N -20°N;110°E -120°E） in April, May, and June 2022 show that, compared with those of temperature, the CC of the specific humidity is less, and the scatter points are not very consistent (Fig. 2). More samples of the FY-3D/VASS specific humidity with abnormally high or low readings appeared in April and June, and the specific humidity value was low on average. In May and June, the CC was low and the high scatter density was distributed below the regression line. The MB in June was relatively low: -0.15 g kg^{-1} (Fig. 2c). From April to June, the average MB was -0.53 g kg^{-1}, MAE was 2.25 g kg^{-1}, and RMSE was 2.97 g kg^{-1} (Fig. 2d).

The study shows that the 340 K of the regional average pseudo-equivalent potential temperature at 850 hPa is the threshold of the onset of the SCSSM (Shao et al. 2021). The FY-3D/VASS temperature and specific humidity at 850hPa in the SCSSM region were a little bit lower than those of ERA5, on average, from April to June. The distribution of equivalent potential temperature at 850 hPa from FY-3D/VASS and ERA5 show that, during the onset of the SCSSM in 2022 from April to June, the pseudo-equivalent potential temperature from FY-3D/VASS is slightly (1-2 K) lower (Fig. 3). Before the onset of the SCSSM in April (Fig. 3a1 and a2), the pseudo-equivalent potential temperature in the SCSSM region was lower than 340 K, and in May, the pseudo-equivalent potential temperature higher than 340 K controls the SCSSM region and the Bay of Bengal (Fig. 3b1 and b2). In June, it further advances northward and reaches South China (Fig. 3c1 and c2). The seasonal distribution and advancement of the pseudo-equivalent potential temperature higher than 340 K of FY-3D/VASS and ERA5 are consistent with each other. FY-3D/VASS data can be used in monitoring, to a certain extent, the change characteristics of large air temperature and humidity changes during the onset of the SCSSM.

3.2 FY-3E/WindRAD evaluation in SCSSM monitoring

In order to analyze its applicability in the monitoring of the SCSSM, FY-3E/WindRAD OWV data was compared with the ocean wind vector from

EUMETSAT's ASCAT on the Metop-C satellite. The time period selected was from 1 April to 30 June 2022, covering the entire process of the onset of the SCSSM. Because the observation time of the two satellites was different, the observation time was about 2200 and 1000 UTC for FY-3E and about 0200 and 1400 UTC for Metop-C in the SCSSM region; therefore, the data are all processed into daily averages data for evaluation, and the daily averages data are matched with spatial grid points in the SCSSM region.

In the monitoring of the SCSSM, attention is paid not only to the wind speed, but also to the meridional wind and zonal wind components. Therefore, these three parameters are evaluated separately. The monthly matching sample number from April to June 2022 was about 20000. The evaluation of zonal wind shows that the CC in April and May were 0.66 and 0.62, respectively (Fig. 4), and the CC in June was relatively lower, at 0.52. The scattered high density area in April was distributed between -5 and 0 m s^{-1}, indicating that the SCSSM region was dominated by easterly wind. The scattered high density area was distributed between -5 m s^{-1} and 5 m s^{-1} in May, changing to 0-5 m s^{-1} in June, indicating the transformation of the zonal wind before and after the onset of the SCSSM. From April to June 2022, on average, the MB of zonal wind was 0.58 m s^{-1}, the MAE was 2.29 m s^{-1}, the RMSE was 3.01 m s^{-1}, and the CC was 0.70 (Fig. 4d). The evaluation of meridional wind shows that the monthly CC from April to June was above 0.75 (Fig. 5), the average CC was 0.85 in the 3 months, and the MB is negative, indicating that the north wind component is slightly stronger than that of Metop-C/ASCAT. The greatest MB was in June. The MAE and RMSE of meridional wind are lower than those of zonal wind, and the difference before and after the onset of the summer monsoon is low. The average MB from April to June was -0.52 m s^{-1}, the MAE was 2.01 m s^{-1}, and the RMSE was 2.70 m s^{-1}. The wind speed evaluation shows that the maximum CC was 0.87 in April (Fig. 6), the average CC from April to June was 0.79, the MB was -0.45 m s^{-1}, the MAE was 1.56 m s^{-1}, and the RMSE was 2.03 m s^{-1}.

According to the monthly average of the ocean surface wind field from April to June 2022 (Fig. 7), the distribution of the ocean surface wind from FY-3E/WindRAD and Metop-C/ASCAT was consistent, and the location and intensity of high wind speed areas were similar. In April (Fig. 7a1 and a2), before the onset of the Asian summer monsoon, there was a northeast wind in the SCSSM region. The wind speed in the northeast of the South China Sea (SCS) and the ocean east of the Philippines was relatively high, and the wind speed from FY-3E/WindRAD was slightly weaker, by 1 m s^{-1}. At this time, the cross-equatorial flow along the east coast of Africa had not been established. The Arabian Sea was controlled by an anticyclone, and southwest wind began to appear in the ocean south of India, extending to the southwest of the Bay of Bengal. In May (Fig. 7b1 and b2), during the process of the successive onset of the Asian summer monsoon in different regions, the cross-equatorial flow along the east coast of Africa was strong and turned westerly or southwesterly in the 0-10°N region extending to the Indochina Peninsula and the northern SCS. The Bay of Bengal summer monsoon and the SCSSM were initiated. It can be seen from the distribution of the wind speed maximum area that the wind speed of FY-3E/WindRAD was slightly lower, by 1 m s^{-1}. In June (Fig. 7c1 and c2), the cross-equatorial flow was further strengthened. The maximum wind speed in the Asian summer monsoon area appeared in the southwest of the Arabian Sea; this was above 11 m s^{-1}. The Asian tropical summer monsoon region was controlled by westerly and southwesterly winds.

It can be seen from the average ocean surface wind speed difference from April to June between FY-3E/WindRAD and Metop-C/ASCAT that the average difference is negative in most areas of the Asian summer monsoon region (Fig. 8a), including the tropical Indian Ocean, south of the equator, and the western Northwest Pacific, partly because of the system deviation caused by the different observation times of the two satellites. The relatively large wind speed difference (about -1.4 m s^{-1}) in the Asian summer monsoon region occurs on the ocean surfaces east of the Philippines, on the western coast of the Bay of Bengal, and in the northern Arabian Sea, and the wind speed difference is relatively small, within the range of 0-10°N. Using the hourly averaged ERA5 10m wind speed from 1 April to 30 June 2022, the diurnal variation of wind speed in the SCSSM region shows that there is a distinct diurnal variation of wind speed ranges about from 3 to 4 m s^{-1}(Fig. 8b). At about 0200 and 1400 UTC, when Metop-C/ASCAT scans the SCSSM region, the wind speeds are

3.80 m s^{-1} and 3.60 m s^{-1} (3.70 m s^{-1} on average), and at about 1000 and 2200 UTC, when FY-3E/WindRAD scans the SCSSM region, the wind speeds are 3.06 m s^{-1} and 3.53 m s^{-1} (3.30 m s^{-1} on average), which is less, by about 0.40 m s^{-1}, than that at Metop-C/ASCAT observation time. Therefore, the negative wind speed difference of FY-3E/WindRAD is partly because of the system deviation caused by the different observation times of the two satellites.

3.3 The SCSSM indices evaluation

The SCSSM regional daily average pseudo-equivalent potential temperature at 850hPa shows that the value of ERA5 is slightly higher than that of FY-3D as a whole (Fig. 9a), and it is significantly higher from mid-March to mid-April. The regional average pseudo-equivalent potential temperature at 850 hPa of ERA5 in mid- March and late March exceeded 340 K. After 28 April, except for 11 and 12 May, it was greater than 340 K, meeting one of the operational indices of the onset of the SCSSM from the NCC, CMA (Shao et al. 2021). The regional average daily pseudo-equivalent potential temperature at 850hPa of FY-3D/VASS also began to exceed 340 K on 28 April, but fell back to below 340 K after 1 May, fluctuated from 8 to 9 May, and remained relatively stable above or near 340 K after 17 May.

The operational monitoring index of the SCSSM of the NCC, CMA uses regional (10°N-20°N; 110-120°E) average zonal wind at 850 hPa. Figure 9b shows the time series of the regional average zonal wind from 1 March to 30 September 2022. It can be seen that the developing trend of the SCSSM index of FY-3E/WindRAD and Metop-C/ASCAT is consistent (10 May), and the onset date of the SCSSM is one day later than that of ERA5 (11 May). The zonal wind direction changed during the onset of the SCSSM in 2022 was well monitored by FY-3E/WindRAD and the combined results of FY-3E/WindRAD and Metop-C/ASCAT.

The former study shows that surface wind can be a better indicator of the onset of the Asian Summer Monsoon system than the wind at 850 hPa (Wu et al. 2013b). From the comparison of FY-3E/WinRAD OWV and ERA5 wind at 850 hPa during the onset of the SCSSM in May 2022 (Fig.10), it can be seen that there is northeast wind near the ocean surface north of the SCSSM in the third pentad of May, during the onset of the SCSSM, but that was not seen in the wind at 850 hPa (Fig. 10a). The definition of monsoon is generally the stable reversal of wind direction and precipitation. The northeast wind monitored by the OWV in the north of the SCS has important indicative significance for the convective activities in the summer monsoon region. In the fourth pentad of May (Fig. 10b), the southwest flow in the north of the SCSSM region is weaker than that in the third pentad of May, but the southwest wind still controls the southern part of the SCSSM region. Similarly, OWV has monitored the ocean surface’s strong northeast wind, which provides important information for the convective monsoon precipitation in the north of the SCS and for determining the onset of the summer monsoon.

3.4 The onset process of the SCSSM in 2022 from FY-3D/E

According to the NCC, CMA, the SCSSM broke out in the third pentad of May, slightly earlier than normal (the fourth pentad in May), and the intensity was close to normal or a little bit weak (note: each pentad is five days; for example, the third pentad in May was from 11 to 15 May; http://cmdp.ncc-cma.net). The SCSSM monitoring indices of pseudo-equivalent potential temperature and ocean surface wind by the FY-3 meteorological satellite also showed that the onset of the SCSSM occurred in the third pentad in May. The characteristics of atmospheric parameters and the onset process of the SCSSM, before and after the onset, were analyzed using FY-3 satellites.

Studies show that the outbreak vortex or cyclone storm in the Bay of Bengal can trigger the onset of the SCSSM in many years (Wu et al. 2011; Ren et al. 2016; Ding and Liu 2001). Before the onset of the SCSSM in 2022, there was tropical storm activity in the Bay of Bengal of the north Indian Ocean. This severe cyclonic storm was named Asani and numbered BOB 03 by the Indian Meteorological Department and 02B by the Joint Typhoon Warning Center, USA (Fig. 11 and 12). There was a tropical depression in the Bay of Bengal on 5 May. It intensified into a tropical storm, was named on 8 May, and then gradually moved to the northwestward. It landed on the coast of the state of Andhra Pradesh, India, on 11 May, and then gradually weakened and dissipated. The maximum intensity reached the Category 1 tropical cyclone intensity recognized by the Joint Typhoon Warning Center and the strong cyclone intensity recognized by the Indian Meteorological Department and CMA. Asani brought strong wind and rainfall to India and Bangladesh, causing at least three deaths, but it failed to significantly alleviate the extreme hot weather in South Asia that began in middle of March and was still developing in early May.

Before the onset of the SCSSM, tropical cyclone activity also occurred in the south Indian Ocean (Fig.11 and 12). A tropical low formed in the central Indian Ocean during 5 May. The system gradually developed and was named Karim on 7 May. Karim tracked southeast, entered the Australian region on 8 May, and intensified, further reaching Category 2 on the intensity scale, with 95 km h^{-1} sustained wind speeds, at 0600 UTC on 8 May. Karim maintained Category 2 intensity during 9 May as the system track steadily southwards. On 10 May, Karim reached peak sustained wind speeds of 110 km h^{-1}, just below Category 3 intensity. Early on 11 May, Karim transitioned to a subtropical system, but continued to produce storm-force winds and gales aided by the strong pressure gradient between the system and a high ridge to the south.

The combined influence of tropical cyclones Karim and Asani increased the intensity of the westerly wind over the Indian Ocean between the 2 cyclones, and the wind speed over the ocean to the south of the Bay of Bengal was more than 10 m s^{-1} in some areas, which promotes a later summer monsoon in the SCS.

Before and after the onset of the SCSSM, the distribution of the average pentad of pseudo-equivalent potential temperature of FY-3D/VASS and ocean surface wind of FY-3E/WindRAD shows that in the first pentad of May (Fig.13), the cross-equatorial flow over the ocean surface along the east coast of Africa was established. Within the latitude range of 0-5°N, there were westerlies in Indian Ocean, and southerlies in the west of the Bay of Bengal. At this time, the SCS was controlled by the northeast wind or easterlies. The wind speed in the north part of the SCS was strong, and there was a low-pressure circulation in the tropical area near 90°E-100°E south of the equator. The low-pressure circulation strengthened the westerly wind to its north. In the second pentad of May, the most typical feature was that in the Bay of Bengal and on the southern hemisphere's ocean surface there were two tropical cyclones, named Asani and Karim, which gradually formed and developed. Affected by the strong storm Asani in the Bay of Bengal, there were easterlies or southeasterlies over the ocean to the south of the SCS and the Indochina Peninsula, merging into the storm Asani. In the third pentad of May, the tropical storm Asani in the Bay of Bengal landed and disappeared; the most obvious feature was that the pseudo-equivalent potential temperature increased in the Indian Peninsula, Bay of Bengal, and Indochina Peninsula. At the same time, the cross-equatorial flow was pulled much stronger by Asani than in the second pentad. The southwest wind controlled the Bay of Bengal and extended eastward to the SCSSM region, causing the onset of the SCSSM. In the fourth pentad of May， the south part of the SCSSM region was continuously controlled by the southwest wind, while the north part was affected by the cold air of the northeast wind. The pseudo-equivalent potential temperature in most regions was higher than 340 K.

The storm in the Bay of Bengal had a pumping effect on the cross-equatorial flow, which made the westerly wind over the tropical ocean north of the equator stronger. After the cyclone storm weakened and disappeared, the strong southwest monsoon crossed the Indochina Peninsula to the SCS, causing the onset of the SCSSM. Although affected by cold air, northeasterly wind appeared in the northern part of the SCS in the fourth pentad of May and the strong southwesterly wind in the north Indian Ocean led the stable southwesterly wind to control the whole SCSSM region after the cold air activity. In the fifth pentad of May, the pseudo-equivalent potential temperature reached higher than 340 K, representing a warm and moist airmass that advanced to South China. Generally, a pseudo-equivalent potential temperature higher than 340 K is classified as the first signs of the summer monsoon. The entire SCS was affected by the southwest summer monsoon, and the southwest and northeast wind met over the ocean to the south of Taiwan. In the sixth pentad of May, the SCS was continuously controlled by the southwest summer monsoon, and the warm and moist airmass was further pushed northward to the Yangtze River basin.

4. Conclusion and discussion

According to the demands of the SCSSM operational monitoring service, in this paper, we carried out an evaluation of FY-3D/VASS temperature and humidity and FY-3E/WindRAD ocean surface wind data in the SCSSM region in April to June. The differences between the atmospheric parameters retrieved by the FY satellites, ERA5, and Metop-C/ASCAT were analyzed. In addition, the SCSSM operational monitoring indices were evaluated. The detailed process of the onset of the SCSSM in 2022 was shown by FY-3 satellite data. The main conclusions are as follows:

(1) The evaluation of FY-3D/VASS temperature and specific humidity at 850hPa compared with that of ERA5 in the SCSSM region averaged from April to June. The temperature MB was -0.64 K, the MAE was 1.09 K, and the RMSE was 1.61 K. The specific humidity MB was -0.53 g kg^{-1}, the MAE was 2.25 g kg^{-1}, and the RMSE was 2.97 g kg^{-1}. The pseudo-equivalent potential temperature calculated by using FY-3D/VASS temperature and specific humidity was slightly lower, by 1-2 K, during the onset of the SCSSM in 2022. The distribution and the seasonal advancement of the pseudo-equivalent potential temperature greater than 340 K from FY-3D/VASS are consistent with that from ERA5, which can be used in monitoring the change of air temperature and humidity during the onset of the SCSSM.

(2) The evaluation of FY-3E/WindRAD OWV, compared with that of Metop-C/ASCAT, averaged from April to June in the SCSSM region, showed that the zonal wind MB was positive, and the meridional wind MB was negative.

The wind speed evaluation shows that the CC was 0.79, the MB was -0.45 m s^{-1}, the MAE was 1.56 m s^{-1}, and the RMSE was 2.03 m s^{-1}. The distribution of the FY-3E/WindRAD and Metop-C/ASCAT ocean surface wind field was consistent, and the location and intensity of high wind speed areas were similar. It can be seen from the horizontal distribution of the average difference from April to June that there was a negative difference in average in most areas of the Asian summer monsoon region, including the tropical Indian Ocean south of the equator and the western Northwest Pacific, partly because of the system deviation caused by the different observation times of the two satellites.

(3) The monitoring indices of the SCSSM, using FY-3D/VASS and FY-3E/WindRAD, show that the two indices are very good at monitoring the pseudo-equivalent potential temperature and zonal wind reversal during the onset of the SCSSM in 2022, which was basically consistent with the onset date officially issued by the NCC, CMA, which was in the third pentad of May. Before the onset of the SCSSM, in early May, the tropical cyclone Karim, in the central Indian Ocean south of the equator, and the storm Asani, in the Bay of Bengal in the north Indian Ocean, pumped the westerly wind near the equator, making the westerly wind in the tropical ocean north of the equator stronger. After the cyclone storm Asani weakened and disappeared, the strong southwesterly monsoon flow crossed the Indochina Peninsula to the SCS, causing the onset of the SCSSM.

In this paper, based on the multiple vertical sounding instruments loaded on the FY polar-orbiting meteorological satellite, the changing characteristics of atmospheric temperature and humidity, before and after the onset of the SCSSM, were monitored. Based on the OWV from the new wind radar instrument on the FY-3E meteorological satellite, the wind field reversal, before and after the onset of the SCSSM, was also monitored. The application ability of the two types of satellite data in the climate monitoring of the SCSSM was demonstrated through various means of verifying the data. In addition to the real-time monitoring of atmospheric parameter changes in the SCSSM region, the polar-orbiting meteorological satellite, with global coverage, can also monitor the cross-equatorial flow, warm and moist air transport, tropical depressions or cyclones in the south Indian Ocean, explosive vortices or tropical storms in the Bay of Bengal, and the triggering effect of synoptic scale systems on the onset of summer monsoon, which are all the important indicators for the establishment of the Asian summer monsoon before the onset of the SCSSM.

According to this study, the operational climate monitoring and forecast of the SCSSM can be carried out using FY meteorological satellites, which can mutually corroborate the results from the meteorological numerical model or reanalysis data, even providing more detailed, near-real-time observation information of the SCSSM's activities. On 1 December 2022, the CMA announced that after six months of trial operation and the "practical" test of this year's flood season, FY-3E and its ground application systems were officially put into operation. FY-3E together with FY-3D will provide higher frequency and more stable observation data for the monitoring and research of the SCSSM.

At present, NSMC, CMA FY-4A satellite datasets are used to monitor the SCSSM in operational work (Yang et al. 2017). The FY-4A AMV is used as the index to monitor the upper troposphere zonal wind direction reversal and TBB is used to monitor the convective activities during the summer monsoon season. The addition of the FY-3E/WindRAD and FY-3D/VASS data increases the effectiveness of the monitoring of the lower-level wind field and the monitoring of the atmospheric temperature and humidity fields. After being applied to the operational summer monsoon monitoring, these data will improve the comprehensive monitoring capability of satellite remote sensing of the summer monsoon, including the monitoring capability of high- and low-layer dynamics, thermodynamics, and precipitation, providing more information for summer monsoon activities.

Data Availability Statement

FY-3D/VASS and FY-3E/WindRAD data provided by China National Satellite Meteorological Center, CMA, the Metop-C/ASCAT ocean wind vector data provided by EUMETSAT available at https://www.eumetsat.int/, the ERA5 reanalysis data provided by ECMWF available at https://cds.climate.copernicus.eu and the operational monitoring indices of the

SCSSM in NCC, CMA available at http://cmdp.ncc-cma.net/climate/monsoon.php.

Acknowledgments

We thank the anonymous reviewers for their helpful suggestions for further improving this manuscript. This research is supported by the National Key Research and Development Program of China (2021YFB3900400), and National Natural Science Foundation of China (42175014). We acknowledge EUMETSAT and ECMWF for providing the data.

References

Bolton, D., 1980: The computation of equivalent potential temperature. *Mon. Wea. Rev.,* **108,** 1046-1053, doi:10.1175/1520-0493(1980)108<1046:TCOEPT>2.0.CO;2.

Chan, J. C. L, W. X. Ai, and J. J. Xu, 2002: Mechanisms responsible for the maintenance of the 1998 South China Sea summer monsoon. *J. Meteor. Soc. Japan*, **80(5)**, 1103-1113, doi:10.2151/jmsj.80.1103.

Chen, W., P. Hu, and J. L. Huangfu, 2022: Multi-scale climate variations and mechanisms of the onset and withdrawal of the South China Sea summer monsoon. *Sci. China: Earth Sci.*, **65(6)**, 1030–1046, doi: 10.1007/s11430-021-9902-5.

Ding, Y. H., and C. Y. Li, 1999: *Onset and Evolution of the South China Sea*

Monsoon and its Interaction with the Ocean. China Meteorological Press, 423 pp. (in Chinese)

Ding, Y. H., and Y. J. Liu, 2001: Onset and the evolution of the summer monsoon over the South China Sea during SCSMEX field experiment in 1998. *J. Meteor. Soc. Japan*, **79**, 255–276, doi:10.2151/jmsj.79.255.

Gu, S. Y., Z. Z. Wang, J. Li, and S. W. Zhang, 2010: The radiometric characteristics of sounding channels for FY-3A/MWHS. *J. Appl. Meteor. Sci.,* **21(3)**, 335-341. (in Chinese)

Guo, P. W., Q. G. Zhu, and X. F. Liu, 1999: Climatological features of convection onset and advancing over Asian tropical region. *J. Nanjing Inst. Meteor.*, **22(3)**, 305-311. (in Chinese)

Guo, Y., N. M. Lu, S. Gu, J. Y. He, and Z. Z. Wang, 2014: Radiometric characteristics of FY-3C microwave humidity and temperature sounder. *J. Appl. Meteor. Sci.*, **25(4)**, 436-444. (in Chinese)

He, J. H., Q. G. Zhu, and M. Murakami, 1996: TBB data-reveled features of Asian-Australian monsoon seasonal transition and Asian summer monsoon establishment. *J. Trop. Meteor.*, **12(1)**, 34-42. (in Chinese)

Hersbach, H., B. Bell, P. Berrisford, S. Hirahara, A. Horányi, J. Muñoz-Sabater, J. Nicolas, C. Peubey, R. Radu, D. Schepers, A. Simmons, C. Soci, S. Abdalla, X. Abellan, G. Balsamo, P. Bechtold, G. Biavati, J. Bidlot, M. Bonavita, G. D. Chiara, P. Dahlgren, D. Dee, M. Diamantakis, R. Dragani, J. Flemming, R. Forbes, M. Fuentes, A. Geer, L.

Haimberger, S. Healy, R. J. Hogan, E. Hólm, M. Janisková, S. Keeley, P. Laloyaux, P. Lopez, C. Lupu, G. Radnoti, P. D. Rosnay, I. Rozum, F. Vamborg, S. Villaume, and J. Thépaut, 2020: The ERA5 global reanalysis. *Quart. J. Roy. Meteor. Soc.*, **46(730)**, 1999-2049, doi:10.1002/qj.3803.

Jiang, N. B., and H. B. Luo, 1995: The first transition of the circulation in Asia around mid-May from 7-year mean ECMWF data. *J. Trop. Meteor.*, **1(1)**, 34-45.

Jiang, J. X., D. Y. Qin, and C. X. Liu, 2006: A primary study of summer monsoon index over the South China Sea and east Asia based on satellite observation. *J. Trop. Meteor.*, **22(5)**, 423-430. (in Chinese)

Lau, K. M., H. T. Wu, and S. Yang, 1998: Hydrologic processes associated with the first transition of the Asian summer monsoon: A pilot satellite study. *Bull. Amer. Meteor. Soc.*, **79**, 1871-1882, doi:10.1175/1520-0477(1998)079%3C1871:HPAWTF%3E2.0.CO;2.

Li, C. Y., and L. P. Zhang, 1999: Characteristics and indices of the South China Sea summer monsoon. *Prog. Nat. Sci.,* **9(6)**, 536-541. (in Chinese)

Liang, J. Y., S. S. Wu, and J. P. You, 1999: The research on variation of onset time of the SCS summer monsoon and its intensity. *J. Trop. Meteor.*, **15(2)**, 97-105. (in Chinese)

Liu, X., A. Xie, Y. Qian, and M. Murakami, 1998: The climate characteristics of summer monsoon onset over South China Sea. *J. Trop. Meteor.*, **14(1)**, 28-37. (in Chinese)

OSI SAF/EARS Winds Team, 2021: *ASCAT Wind Product User Manual*, 28 pp. [Available at https://scatterometer.knmi.nl/publications/pdf/ASCAT_Product_Manual.pdf]

Qian, W. H., and Y. F. Zhu, 2001: Study on the deep convection characteristics of Asian summer monsoon onset. *Acta Meteor. Sin.*, **59(5)**, 578-590. (in Chinese)

Ren, S. L., and X. Fang, 2013: The application of AMV and TBB in monitoring the South China Sea summer monsoon. *J. Trop. Meteor.*, **29(6)**, 1051-1056. (in Chinese)

Ren, S. L., Y. M. Liu, and G. X. Wu, 2016: Statistical characteristics of the tropical cyclone activities over the Northwest Pacific and the Bay of Bengal during the Asian summer monsoon onset. *Acta Meteor. Sin.*, **74(6)**, 837-849, doi:10.11676/qxxb2016.067.

Ren, S. L., J. Y. Jiang, Y. Li, and X. J. Wu, 2017: *Technical Guide for Monitoring the Onset of South China Sea Summer Monsoon by Satellite Remote Sensing Products (QX/T 379-2017)*. China Meteorological Press, 6 pp. (in Chinese)

Ren, S. L., Y. Li, X. Fang, and J. Y. Jiang, 2018: The South China Sea summer monsoon onset index using FY satellite derived data. *J. Trop. Meteor.*, **34(5)**, 587-597, doi:10.16032/j.issn.1004-4965.2018.05.002.

Ren, S. L., N. Niu, D. Y. Qin, B. Y. Yang, R. H. Xu, and D. Xian, 2022: Extreme cold and snowstorm event in North America in February 2021 based on satellite data. *J. Appl. Meteor. Sci.*, **33(6)**, 696-710. (in Chinese)

Shao, X., Y. J. Liu, Y. Yuan, H. Gao, Y. F. Zhu, and X. Z. Zhang, 2021: *Monitoring Indicators of South China Sea Summer Monsoon (QX/T 633-2021)*. China Meteorological Press, 5 pp. (in Chinese)

Verhoef, A., M. Portabella and A. Stoffelen, 2012: High-resolution ASCAT scatterometer winds near the coast. *IEEE Trans. Geosci. Remote Sens.*, **50(7)**, 2481-2487,doi:10.1109/TGRS.2011.2175001.

Verspeek, J., M. Portabella, A. Stoffelen and A. Verhoef, 2019: *ASCAT Calibration and Validation, OSI SAF Technical Report,* SAF/OSI/CDOP/KNMI/TEC/TN/163, 24 pp. [Available at https://scatterometer.knmi.nl/publications/pdf/osisaf_cdop3_ss3_valrep_ascat_c_winds_1.3.pdf]

Wang, B., 2008: Thrusts and prospects on understanding and predicting Asian monsoon climate. *Acta Meteor. Sin.*, **22(4)**, 383-403.

Wang, H., F. Liu, and B. Wang, T. Li, 2018: Effects of intraseasonal oscillation on South China Sea summer monsoon onset. *Climate Dyn.*, **51**, 2543-2558, doi:10.1007/ s00382-017-4027-9.

Webster, P. J., and S. Yang, 1992; Monsoon and ENSO: Selective systems. *Quart. J. Roy. Meteor. Soc.*, **118(507)**, 877-926, doi:10.1002/qj.49711850705.

Wu, G. X, and Y. S. Zhang, 1998: Tibetan Plateau forcing and the timing of the monsoon onset over South Asia and the South China Sea. *Mon. Wea. Rev.*,

126(4),913-927,doi:10.1175/1520-0493(1998)126<0913:TPFATT>2.0.CO;2

Wu, G. X., Y. Guan, T. M. Wang, Y. M. Liu, J. H. Yan, and J. Y. Mao, 2011: Vortex genesis over the Bay of Bengal in spring and its role in the onset of the Asian summer monsoon. *Sci. China: Earth Sci.*, **54**, 1-9, doi: 10.1007/s11430-010-4125-6.

Wu, G. X., Y. M. Liu, B. He, Q. Bao, A. M. Duan, and F. F. Jin, 2012: Thermal controls on the Asian summer monsoon. *Sci. Rep.*, 2:404, doi: 10.1038/srep00404.

Wu, G. X., S. L. Ren, J. M. Xu, D. X. Wang, Q. Bao, B. Q. Liu, and Y. M. Liu, 2013a: Impact of tropical cyclone development on the instability of South Asian High and the summer monsoon onset over Bay of Bengal. *Climate Dyn.*, **41**, 2603-2616, doi:10.1007/s00382-013-1766-0.

Wu, G. X., A. M. Duan, Y. M. Liu, J. H. Yan, B. Q. Liu, S. L. Ren, Y. N. Zhang, T. M. Wang, X. Y. Liang, and Y. Guan, 2013b: Recent advances in the study on the dynamics of the Asian Summer Monsoon onset. *Chin. J. Atmos. Sci.,* **37(2)**, 211-228, doi:10.3878/j.issn.1006-9895.2012.12312.

Xian, D., P. Zhang, L. Gao, R. J. Sun, H. Z. Zhang, and J. Xu, 2021: FengYun meteorological satellite products for earth system science applications. *Adv. Atmos. Sci.*, **38(8)**, 267-1284, doi:10.1007/s00376-021-0425-3.

Xu, P. Q., L. Wang, W. Chen, J. Feng, and Y. Y. Liu, 2019: Structural changes in the Pacific–Japan pattern in the late 1990s. *J. Climate*, **32**, 607-621, doi:10.1175/JCLI-D-18-0123.1.

Yang, J., Z. Zhang, C. Wei, F. Lu, and Q. Guo, 2017: Introducing the new generation of Chinese geostationary weather satellites, Fengyun-4. *Bull. Amer. Meteor. Soc.*, 98, 1637-1658, doi:10.1175/BAMS-D-16-0065.1.

Zhang, Q. Y., S. Y. Tao, and L. T. Chen, 2003: The inter-annual variability of East Asian summer monsoon indices and its association with the pattern of general circulation over East Asia. *Acta Meteor. Sin.*, **61(4)**, 559-568. (in Chinese)

Zhang, P., H. Yang, H. Qiu, G. Ma, Z. D. Yang, N. M. Lu, and J. Yang, 2021: Quantitative remote sensing from the current FengYun 3 satellites. *Adv. Meteor. Sci. Technol.*, **2(4)**, 6-11. (in Chinese)

Zhang, P., X. Q. Hu, Q. F. Lu, A. J. Zhu, M. Y. Lin, L. Sun, L. Chen, and X. Na, 2022: FY-3E: the first operational meteorological satellite mission in an early morning orbit. *Adv. Atmos. Sci.*, **39(1)**, 1-8, doi:10.1007/s00376-021-1304-7.

Zhu, Y. F., G. L. Lin, and W. H. Qian, 2001: Comparision of the SCS summer monsoon onset characteristics derived from different datasets. *J. Trop. Meteor.*, **17(1)**, 34-44. (in Chinese)

Zhuang, G. T., 2022: *Technical Review of National High Impact Weather Monitoring and Forecasting Service (2021)*. China Meteorological Press, 309 pp. (in Chinese)

List of Figures

Fig.1. The scatter density and evaluation indices of temperature at 850 hPa between FY-3D/VASS and ERA5 in the SCSSM region (10°N -20°N; 110°E -120°E） in April (a), May (b), and June (c), and the average of April, May, and June (d) 2022.

Fig.2. The scatter density and evaluation indices of specific humidity at 850 hPa between FY-3D/VASS and ERA5 in the SCSSM region (10°N -20°N; 110°E -120°E） in April (a), May (b), and June (c), and the average of April, May, and June (d) 2022.

Fig.3. The monthly mean θ_{se} (unit: K) at 850 hPa from ERA5 (a1, b1, and c1) and FY-3D/VASS (a2, b2, and c2) in April, May, and June 2022.

Fig.4. The scatter density and evaluation indices of ocean surface zonal wind between FY-3E/WindRAD and Metop-C/ASCAT in the SCSSM region (10°N -20°N; 110°E -120°E) in April (a), May (b), and June (c), and the average of April, May, and June (d) 2022.

Fig.5. The scatter density and evaluation indices of ocean surface meridional wind between FY-3E/WindRAD and Metop-C/ASCAT in the SCSSM region (10°N -20°N; 110°E -120°E) in April (a), May (b), and June (c), and the average of April, May, and June (d) 2022.

Fig.6. The scatter density and evaluation indices of ocean surface wind speed between FY-3E/WindRAD and Metop-C/ASCAT in the SCSSM region (10°N

-20°N; 110°E -120°E) in April (a), May (b), and June (c), and the average of April, May, and June (d) 2022.

Fig.7. Monthly mean OWV wind stream and wind speed (m s^{-1}) from Metop-C/ASCAT (a1, b1, and c1) and FY-3E/WindRAD(a2, b2, and c2) in April, May, and June 2022.

Fig.8. Average OWV wind speed difference (m s^{-1}) between FY-3E/WindRAD and Metop-C/ASCAT from April to June 2022 (a) and the average diurnal variation of 10m wind speed from ERA5 in April, May, and June 2022 in the SCSSM region (10°N -20°N; 110°E -120°E) (b); the blue and red numbers indicate Metop-C/ASCAT and FY-3E/WindRAD observation times, respectively.

Fig.9. The time series of daily mean θ_{se} (unit: K) at 850 hPa from FY-3D/VASS and ERA5 (a) and ocean surface zonal wind (unit: m s^{-1}) from FY-3E/WindRAD, Metop-C/ASCAT, and ERA5 (b) in the SCSSM region from 1 March to 30 September 2022.

Fig.10. Average wind vectors in third pentad of May (a) and fourth pentad of May (b) 2022 from FY-3E/WindRAD OWV (red) and ERA5 wind at 850hPa (blue).

Fig.11. Tracks of Indian Ocean tropical cyclones Asani (red color) and Karim (blue color) in May 2022 and elevation (shaded, unit: m); the numbers indicate the times of tropical cyclone activity (0506-12:00 indicates 1200 UTC 6 May, for example).

Fig.12. FY-3E/WindRAD OWV on 3 May (a1) and 8 May (b1); the combined result of FY-3E/WindRAD and Metop/ASCAT OWV on 3 May (a2) and 8 May (b2); and FY-4A Satellite images of Indian Ocean cyclone Asani and Karim on 3 May (c) and 8 May (d) 2022 (shaded: wind speed, m s^{-1})

Fig.13. Average pentad of FY-3D/VASS θ_{se} at 850 hPa (shaded, unit: K) and FY-3E/WindRAD OWV (vector) from the first to sixth pentads (a to f) of May 2022.

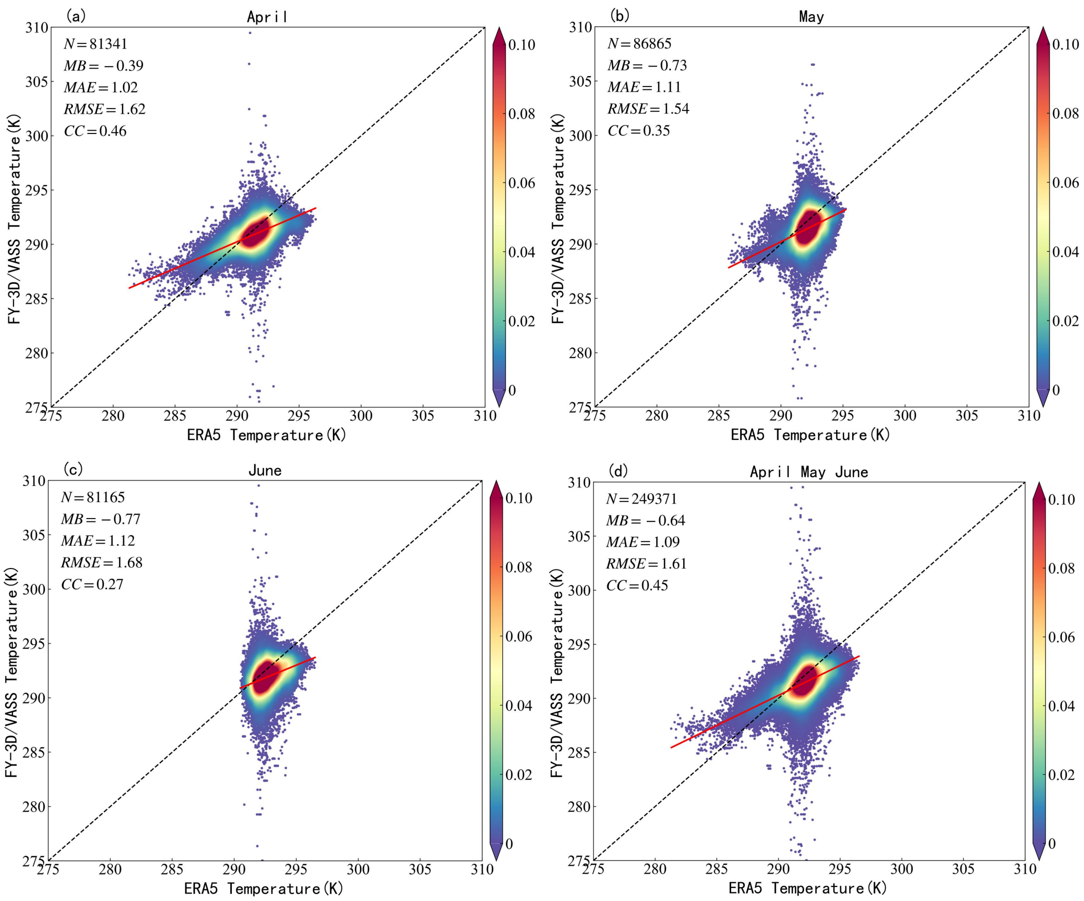

Fig.1. The scatter density and evaluation indices of temperature at 850 hPa between FY-3D/VASS and ERA5 in the SCSSM region (10°N -20°N; 110°E -120°E） in April (a), May (b), and June (c), and the average of April, May, and June (d) 2022.

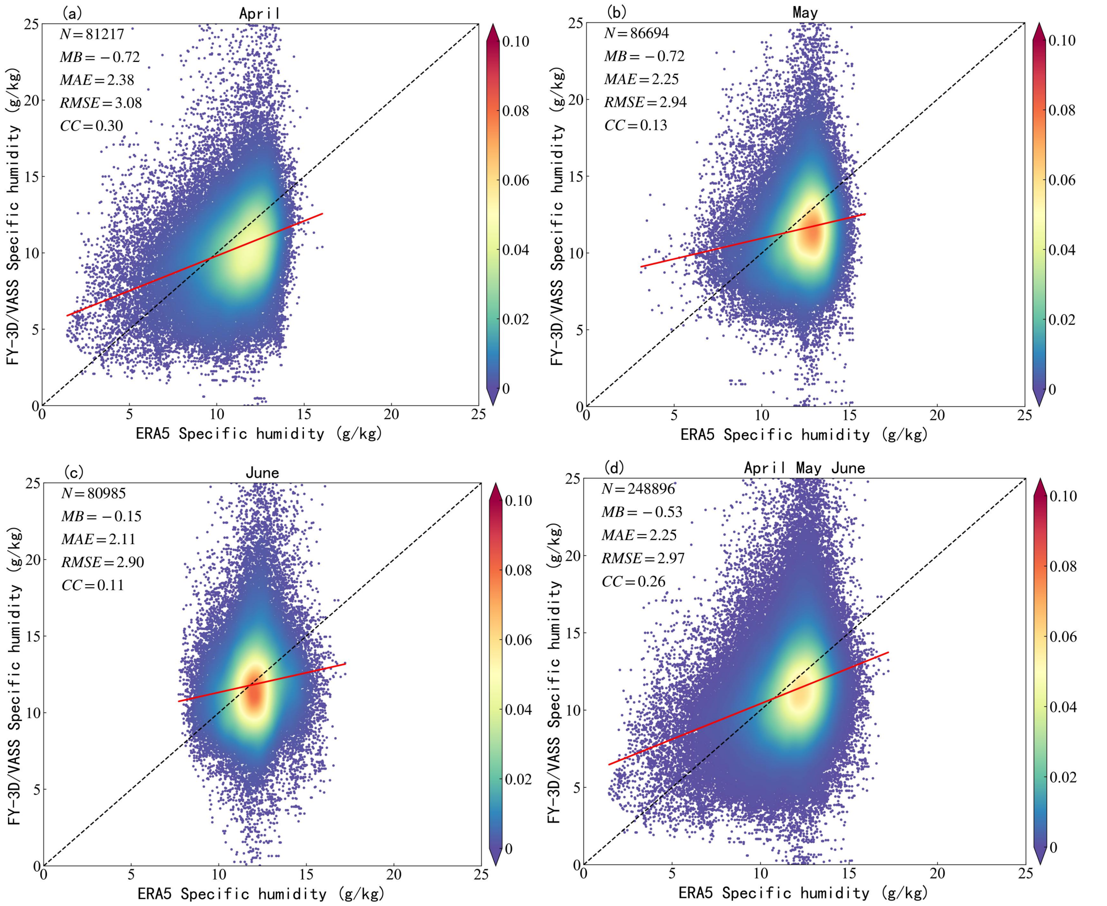

Fig.2. The scatter density and evaluation indices of specific humidity at 850 hPa between FY-3D/VASS and ERA5 in the SCSSM region (10°N -20°N; 110°E -120°E）in April (a), May (b), and June (c), and the average of April, May, and June (d) 2022.

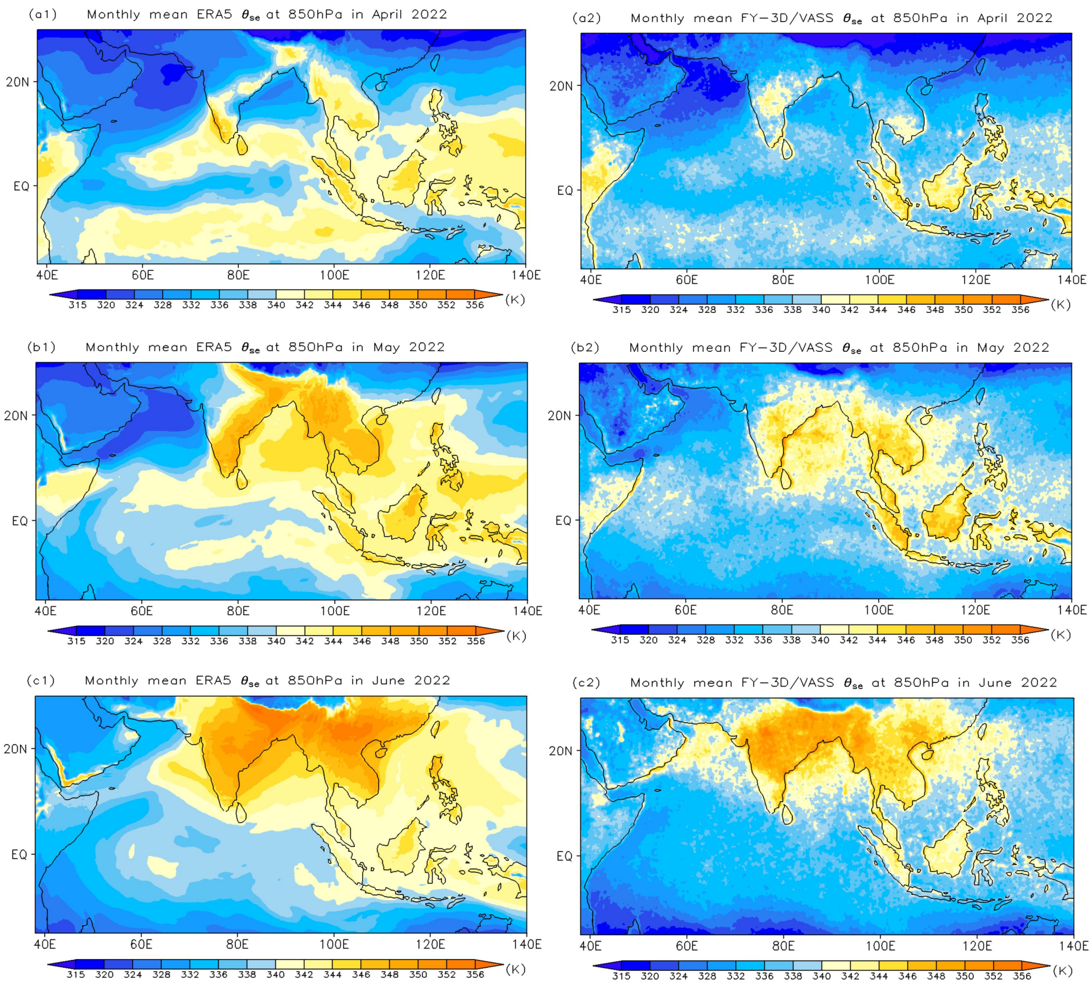

Fig.3. The monthly mean θ_{se} (unit: K) at 850 hPa from ERA5 (a1, b1, and c1) and FY-3D/VASS (a2, b2, and c2) in April, May, and June 2022.

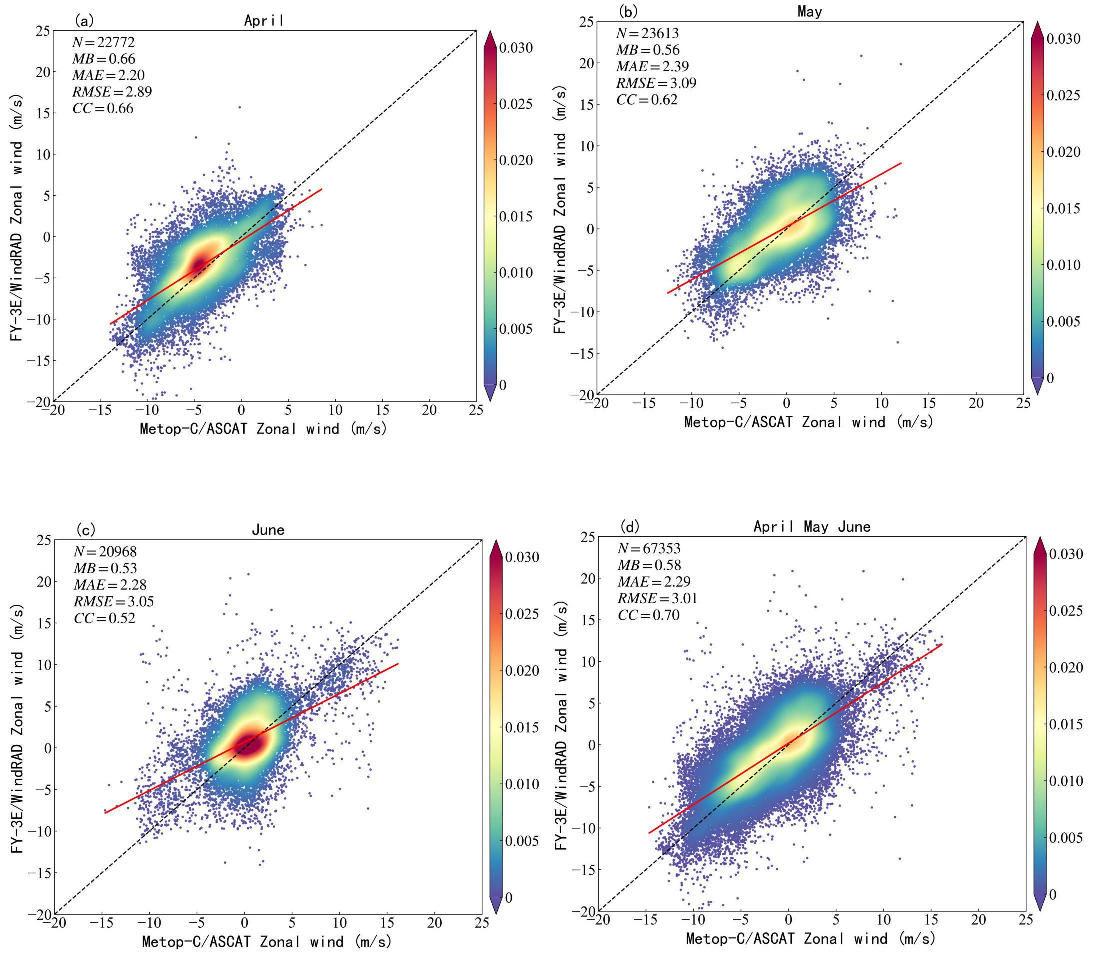

Fig.4. The scatter density and evaluation indices of ocean surface zonal wind between FY-3E/WindRAD and Metop-C/ASCAT in the SCSSM region (10°N -20°N; 110°E -120°E) in April (a), May (b), and June (c), and the average of April, May, and June (d) 2022.

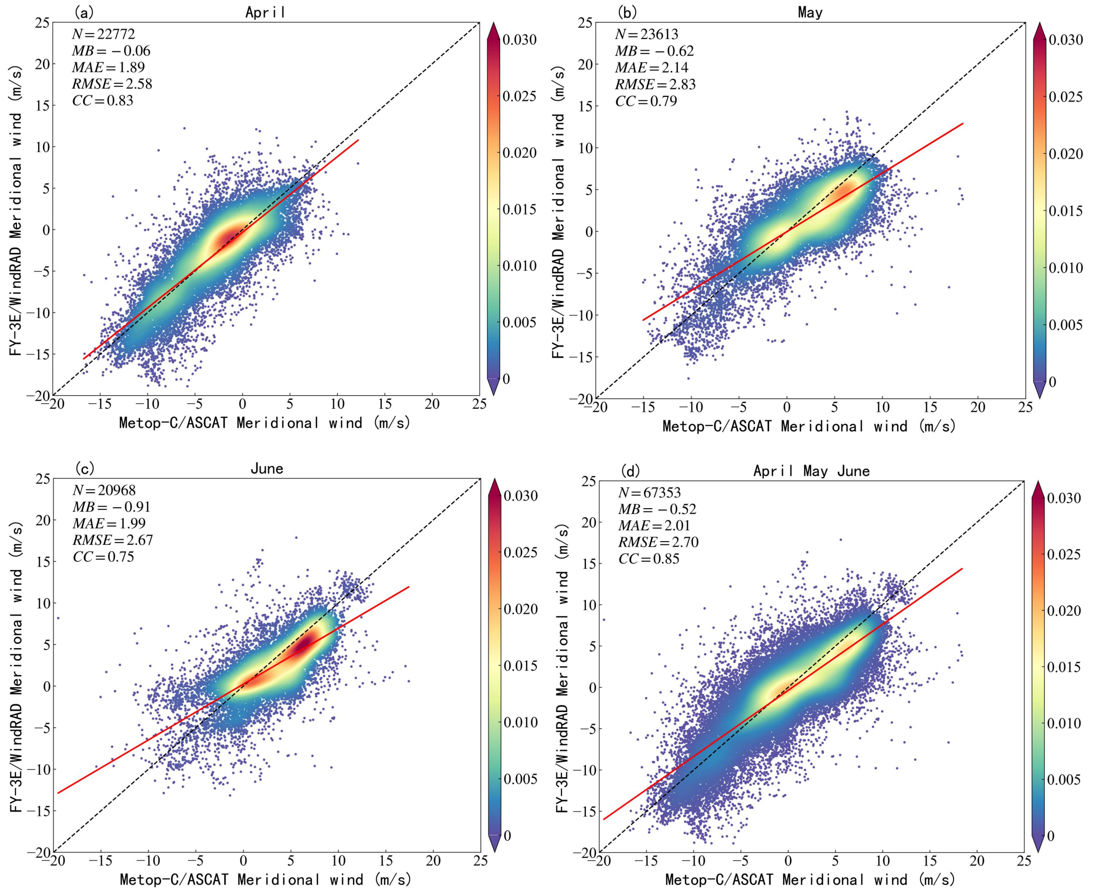

Fig.5. The scatter density and evaluation indices of ocean surface meridional wind between FY-3E/WindRAD and Metop-C/ASCAT in the SCSSM region (10°N -20°N; 110°E -120°E) in April (a), May (b), and June (c), and the average of April, May, and June (d) 2022.

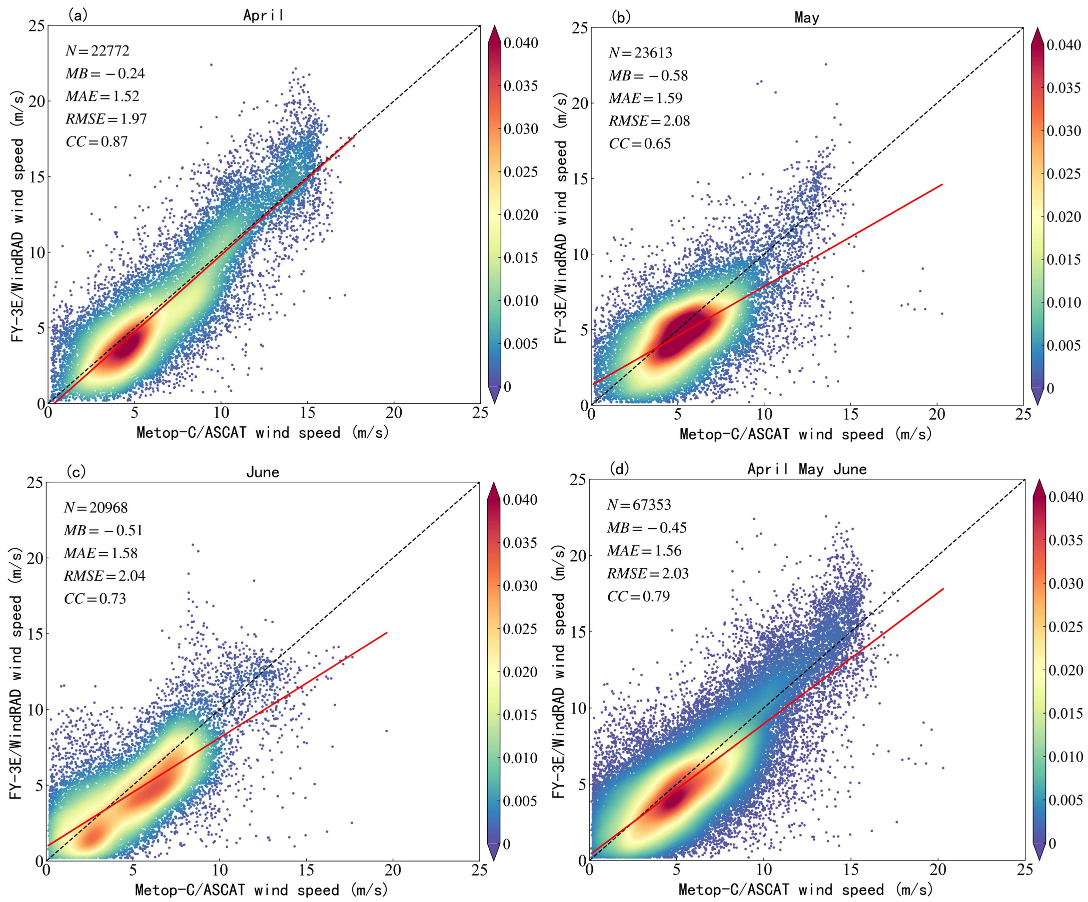

Fig.6. The scatter density and evaluation indices of ocean surface wind speed between FY-3E/WindRAD and Metop-C/ASCAT in the SCSSM region (10°N -20°N; 110°E -120°E) in April (a), May (b), and June (c), and the average of April, May, and June (d) 2022.

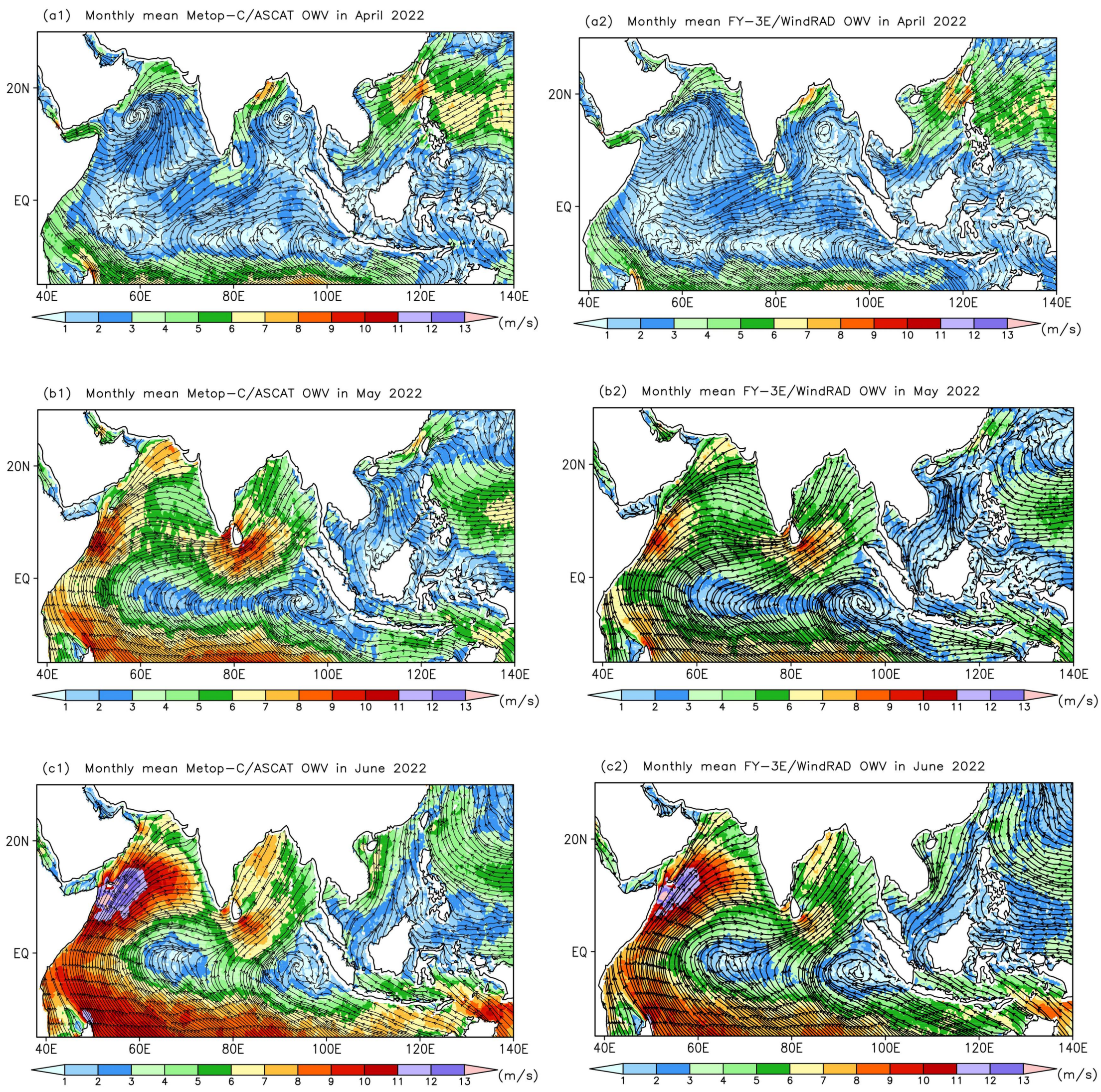

Fig.7. Monthly mean OWV wind stream and wind speed (m s^{-1}) from Metop-C/ASCAT (a1, b1, and c1) and FY-3E/WindRAD(a2, b2, and c2) in April, May, and June 2022.

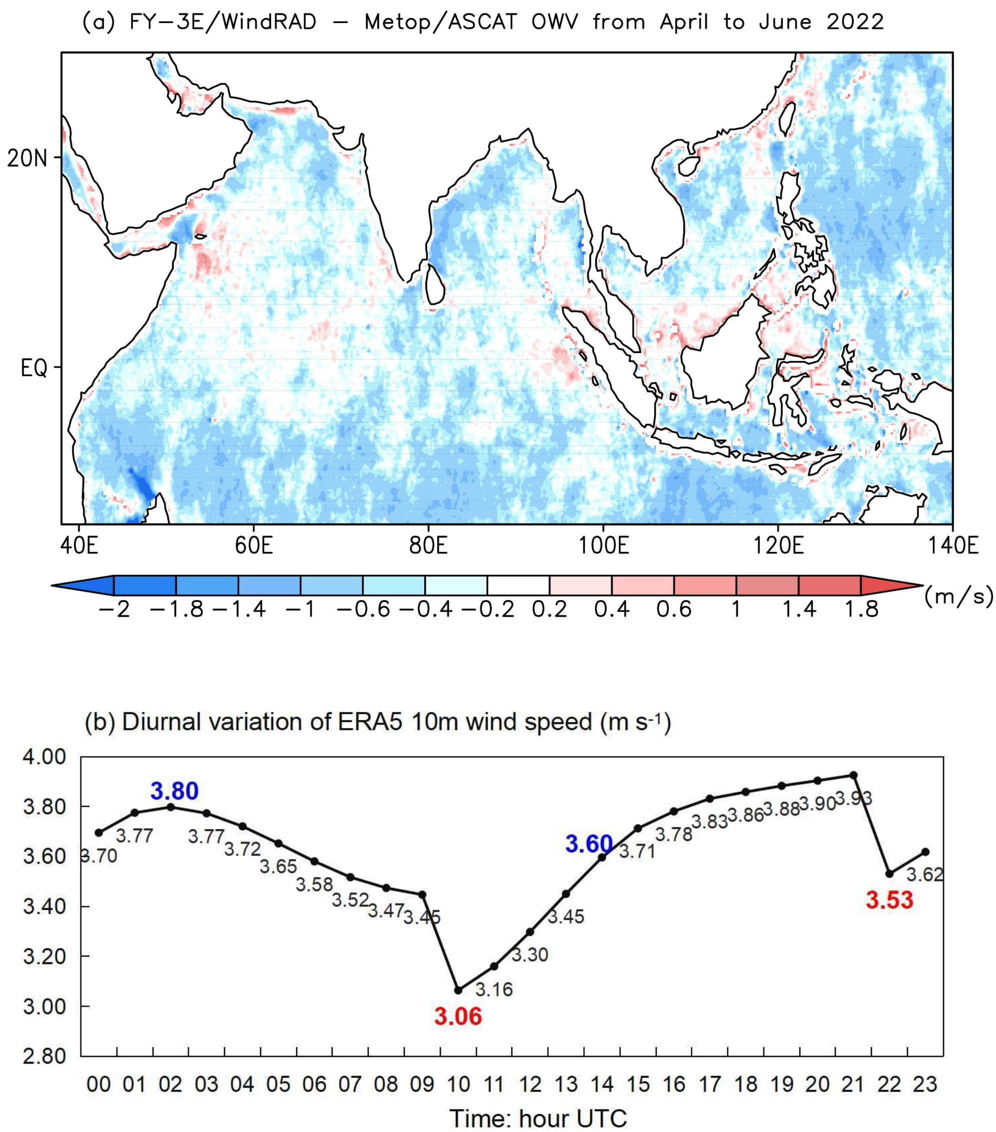

Fig.8. Average OWV wind speed difference (m s^{-1}) between FY-3E/WindRAD and Metop-C/ASCAT from April to June 2022 (a) and the average diurnal variation of 10m wind speed from ERA5 in April, May, and June 2022 in the SCSSM region (10°N -20°N; 110°E -120°E) (b); the blue and red numbers indicate Metop-C/ASCAT and FY-3E/WindRAD observation times, respectively.

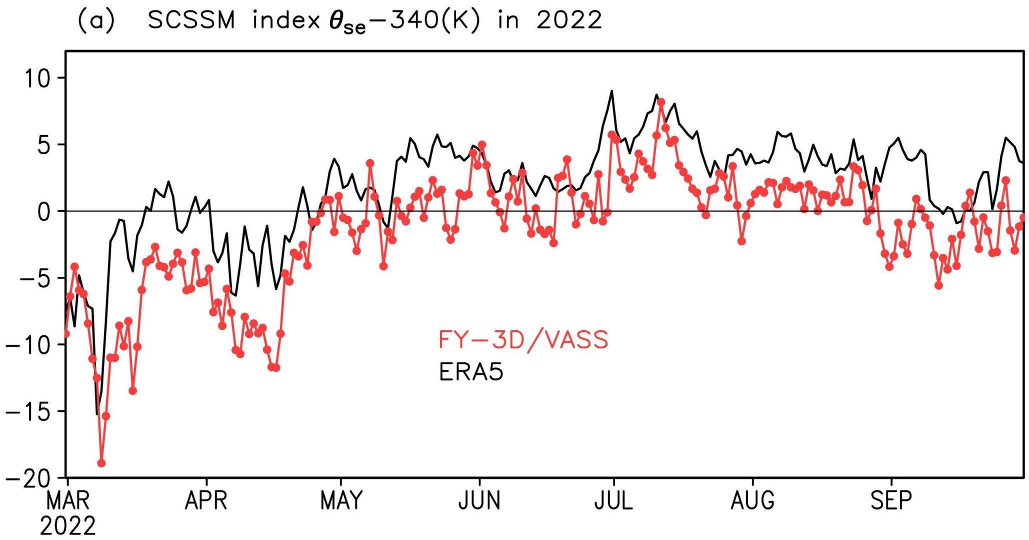

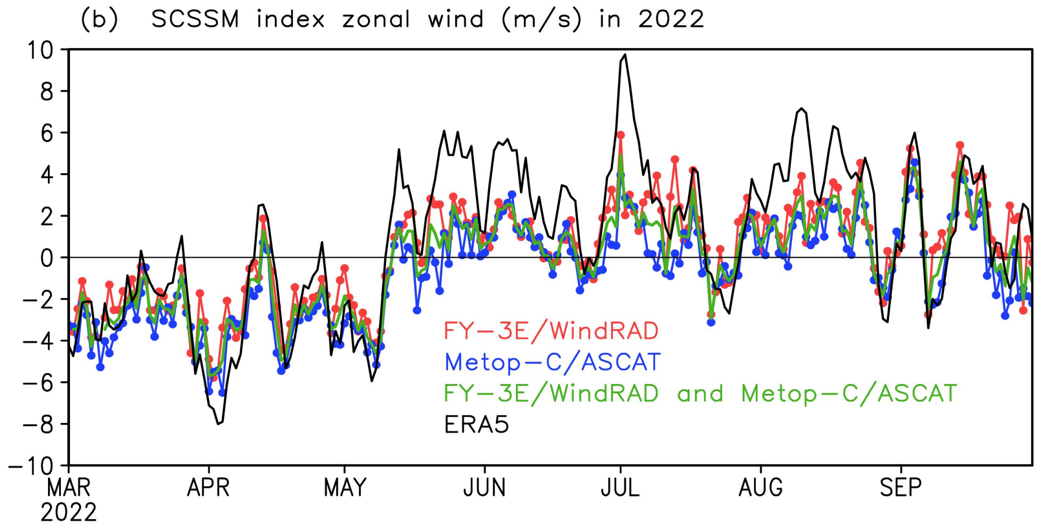

Fig.9. The time series of daily mean θ_{se} (unit: K) at 850 hPa from FY-3D/VASS and ERA5 (a) and ocean surface zonal wind (unit: m s^{-1}) from FY-3E/WindRAD, Metop-C/ASCAT, and ERA5 (b) in the SCSSM region from 1 March to 30 September 2022.

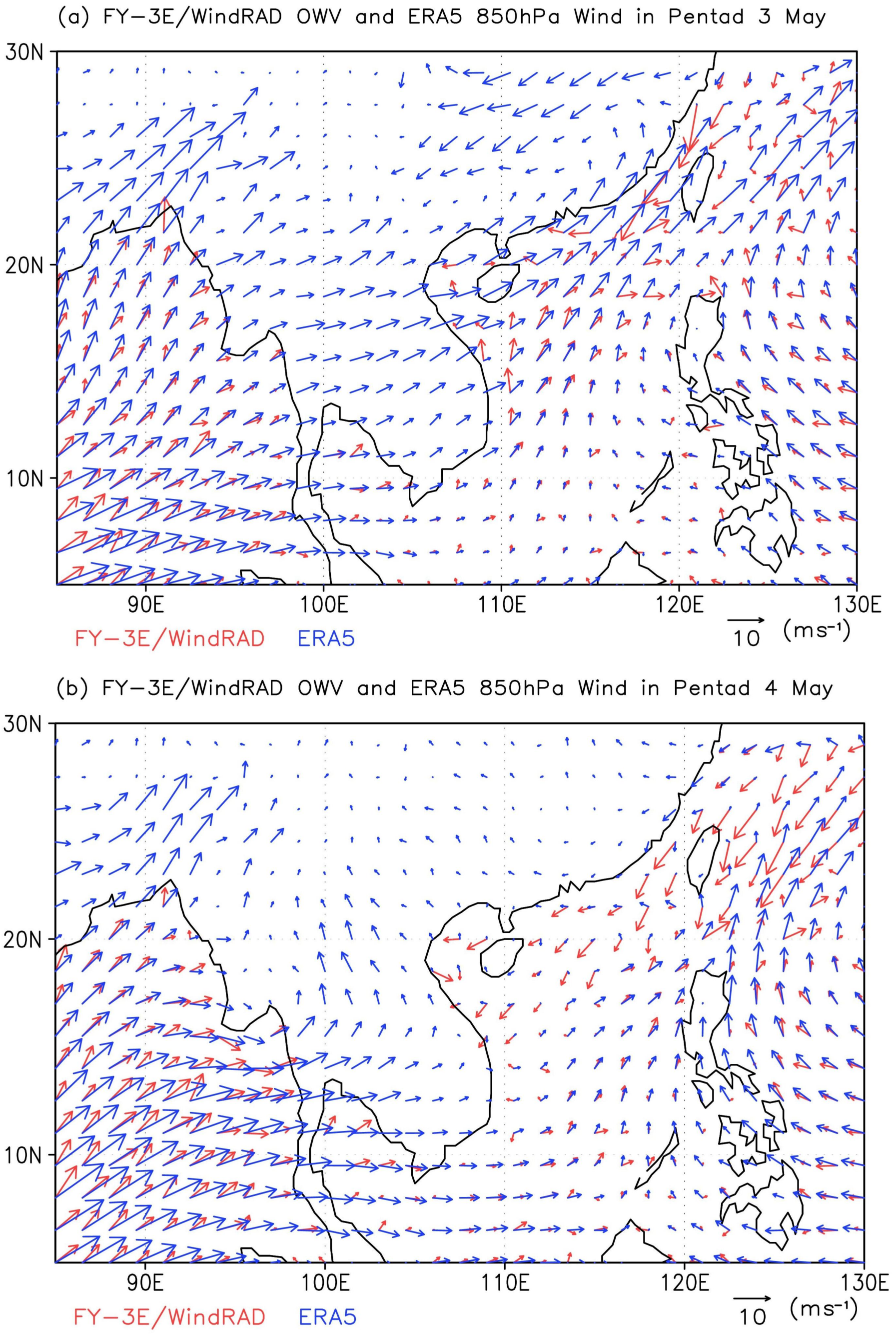

Fig.10. Average wind vectors in third pentad of May (a) and fourth pentad of May (b) 2022 from FY-3E/WindRAD OWV (red) and ERA5 wind at 850hPa (blue).

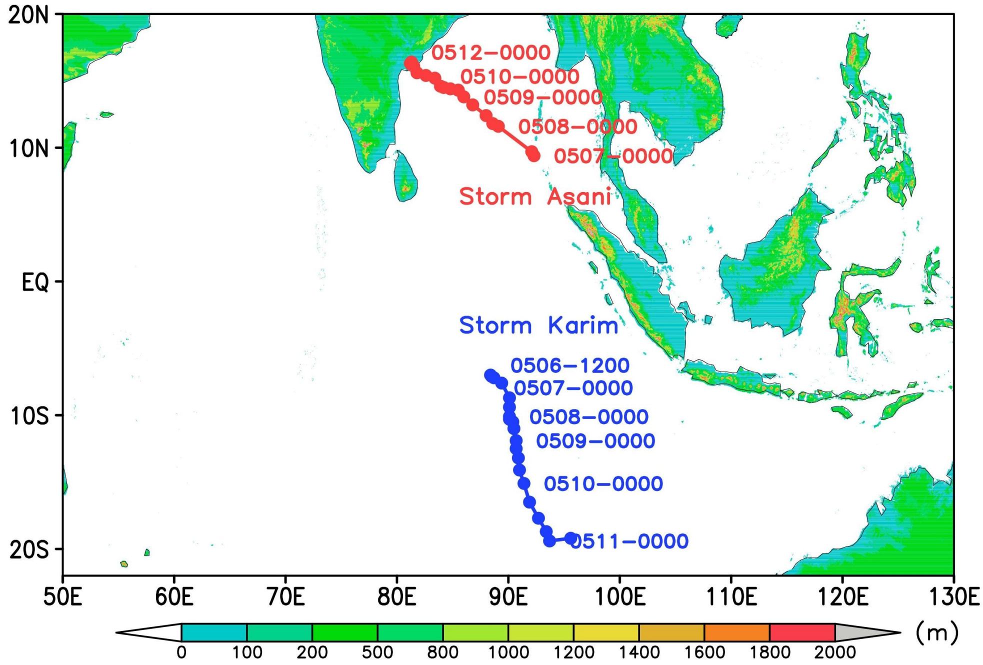

Fig.11. Tracks of Indian Ocean tropical cyclones Asani (red color) and Karim (blue color) in May 2022 and elevation (shaded, unit: m); the numbers indicate the times of tropical cyclone activity (0506-12:00 indicates 1200 UTC 6 May, for example).

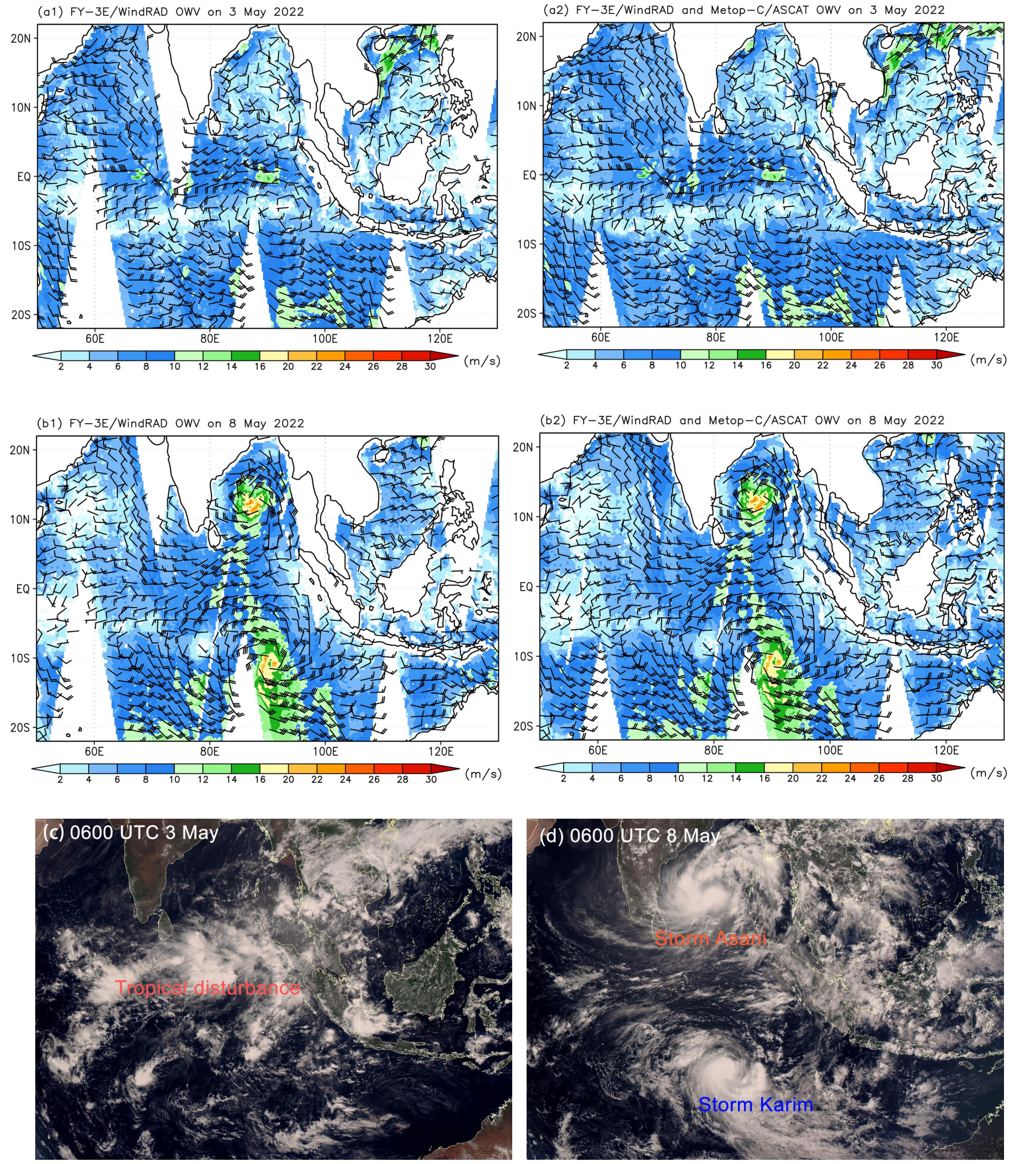

Fig.12. FY-3E/WindRAD OWV on 3 May (a1) and 8 May (b1); the combined result of FY-3E/WindRAD and Metop/ASCAT OWV on 3 May (a2) and 8 May (b2); and FY-4A Satellite images of Indian Ocean cyclone Asani and Karim on 3 May (c) and 8 May (d) 2022 (shaded: wind speed, m s^{-1}).

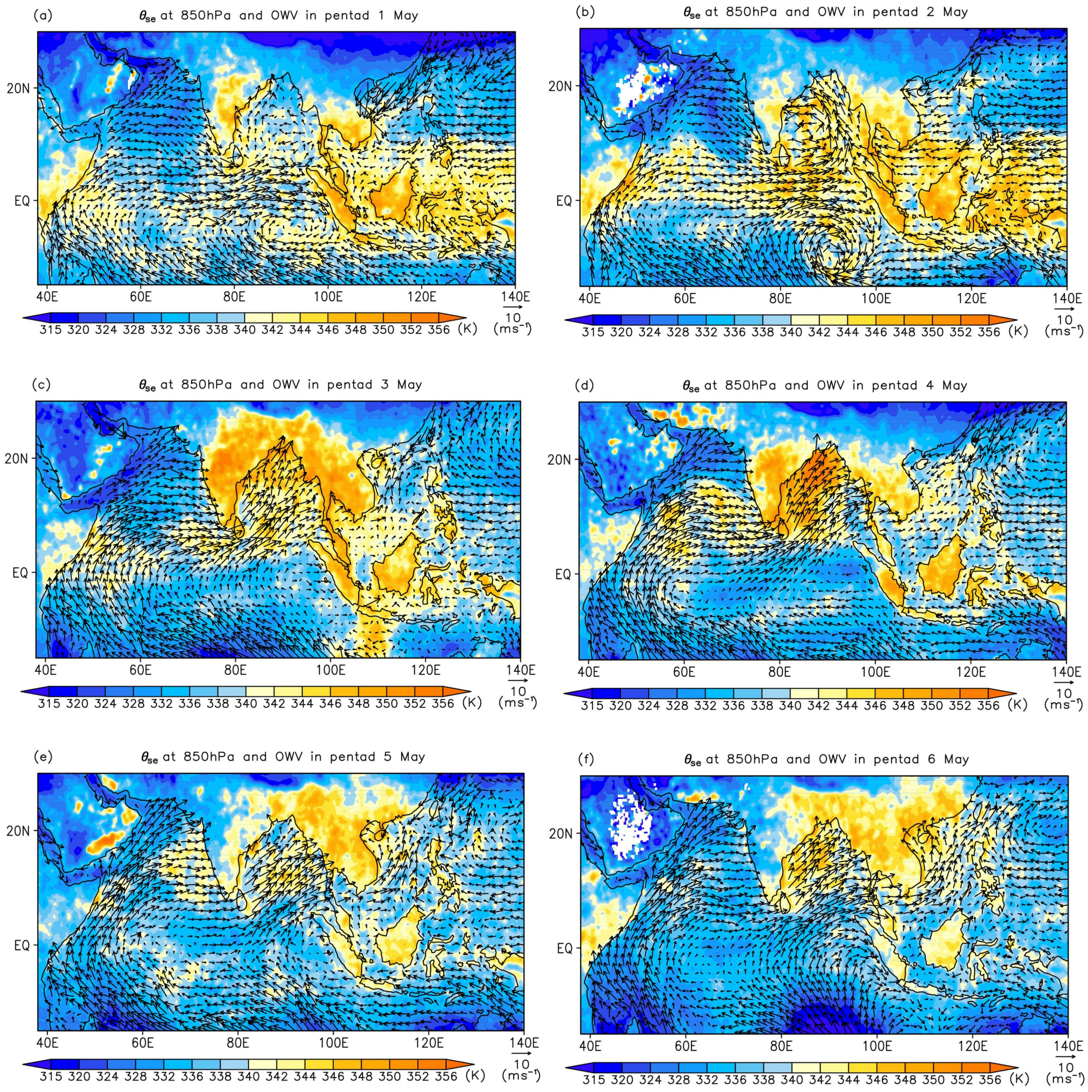

Fig.13. Average pentad of FY-3D/VASS θ_{se} at 850 hPa (shaded, unit: K) and FY-3E/WindRAD OWV (vector) from the first to sixth pentads (a to f) of May 2022.